

View-Invariant, Occlusion-Robust Probabilistic Embedding for Human Pose

Ting Liu^{1,*} · Jennifer J. Sun^{2,*} · Long Zhao^{1,3} · Jiaping Zhao¹ ·
Liangzhe Yuan¹ · Yuxiao Wang¹ · Liang-Chieh Chen¹ · Florian Schroff¹ ·
Hartwig Adam¹

Received: date / Accepted: date

Abstract Recognition of human poses and activities is crucial for autonomous systems to interact smoothly with people. However, cameras generally capture human poses in 2D as images and videos, which can have significant appearance variations across viewpoints. To address this, we explore recognizing similarity in 3D human body poses from 2D information, which has not been well-studied in existing works. Here, we propose an approach to learning a compact view-invariant em-

bedding space from 2D body joint keypoints, without explicitly predicting 3D poses. Input ambiguities of 2D poses from projection and occlusion are difficult to represent through a deterministic mapping, and therefore we use probabilistic embeddings. In order to enable our embeddings to work with partially visible input keypoints, we further investigate different keypoint occlusion augmentation strategies during training. Experimental results show that our embedding model achieves higher accuracy when retrieving similar poses across different camera views, in comparison with 3D pose estimation models. We further show that keypoint occlusion augmentation during training significantly improves retrieval performance on partial 2D input poses. Results on action recognition and video alignment demonstrate that our embeddings, without any additional training, achieves competitive performance relative to other models specifically trained for each task.

Keywords Human Pose Embedding · Probabilistic Embedding · View-Invariant Pose Retrieval · Occlusion-Robustness

Ting Liu
E-mail: liuti@google.com

Jennifer J. Sun
E-mail: jjsun@caltech.edu

Long Zhao
E-mail: lz311@cs.rutgers.edu

Jiaping Zhao
E-mail: jiapingz@google.com

Liangzhe Yuan
E-mail: lzyuan@google.com

Yuxiao Wang
E-mail: yuxiaow@google.com

Liang-Chieh Chen
E-mail: lcchen@google.com

Florian Schroff
E-mail: fschroff@google.com

Hartwig Adam
E-mail: hadam@google.com

¹ Google Research, CA, USA.

² California Institute of Technology, CA, USA.

³ Rutgers University, NJ, USA.

* Equal contribution.

1 Introduction

Automatic perception of human poses and activities is an important step towards image and video understanding [15], autonomous vehicles [17], and social robotics [16]. In these applications, perception is often based on monocular cameras, which depict humans in two dimensions. However, when we represent three-dimensional (3D) human poses in two dimensions (2D), the same pose appears different across camera views due to changing relative depth of body parts and self-occlusions. These variations in 2D representations across viewpoints present

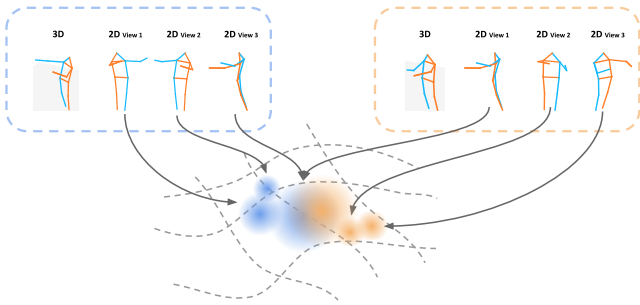


Fig. 1: We embed 2D poses such that our embeddings are (1) view-invariant (2D projections of similar 3D poses are embedded close together) and (2) probabilistic (embeddings are distributions that cover different 3D poses projecting to the same input 2D pose).

a challenge for analyzing human behavior from 2D data. To address this challenge, we explore how well models can recognize similarity of 3D poses using 2D inputs.

We propose to learn view-invariant embeddings for 2D poses, which has not been well-explored in existing works. Typically, embedding models are trained from images using metric learning techniques [47, 22, 10]. However, images with similar human poses can appear different due to a variety of factors, such as viewpoints, subjects, backgrounds, and clothing. As a result, it can be difficult to understand errors in the embedding space from a specific factor of variation. Furthermore, multi-view image datasets for human poses are difficult to capture in the wild with 3D groundtruth poses. Here, we embed 2D pose keypoints to view-invariant embeddings as illustrated in Fig. 1. Our method leverages existing 2D keypoint detectors, similar to 2D-to-3D lifing models [44, 76]. Using 2D keypoints as inputs allows the embedding model to focus on learning view invariance. Our 2D keypoint embeddings can be trained using datasets in lab environments, while having the model generalize to in-the-wild data.

Another aspect of embedding models we aim to address is occlusion-robustness. For models to be applicable in-the-wild, they need to handle pose occlusions that are present in natural images. This ability to embed partial poses is also useful for searching for poses through parts. One simple solution is to train an individual embedding model for each possible occlusion pattern. However, this is infeasible in practice due to the large occlusion diversity of natural human poses. On the other hand, training data for pose models are generally captured in lab environments, and may not contain diverse occlusion patterns. In this paper, we propose to learn a unified occlusion-robust embedding model by synthesizing keypoint visibilities during training. We explore different synthetic keypoint dropout

strategies to enable our model to be robust to common patterns of missing keypoints in-the-wild.

The input ambiguity of 2D poses is addressed by our model using probabilistic embeddings. Many valid 3D poses can be projected to the same or very similar 2D pose [1]. This input uncertainty is difficult to represent using deterministic mappings to the embedding space (point embeddings) [49, 32]. Our embedding space consists of probabilistic embeddings based on multivariate Gaussian. We show that the learned variance from our method correlates with input 2D ambiguities.

Since poses describe body configurations or actions, one direct application of our embeddings is pose-based image retrieval. Our embeddings enable users to search images by fine-grained fully or partially visible pose, such as jumping with hands up, riding bike with one hand waving, and many other actions that are potentially difficult to pre-define. The importance of this application is further highlighted by works such as [47, 29]. Compared with using 3D keypoints with alignment for retrieval, our embedding enables efficient similarity comparisons in Euclidean space. Our embeddings can also be applied to other tasks where recognizing pose similarity across views is important. Here, we demonstrate our embedding performance on action recognition [75, 26] and video alignment [14].

Contributions We have developed a framework for mapping 2D poses to probabilistic embeddings where (1) 2D pose embedding distances correspond to their similarities in absolute 3D pose space, (2) a single model embeds different pose visibility patterns, such as those from occlusions, and (3) probabilistic embeddings capture input ambiguity. We evaluate our embeddings on cross-view pose retrieval, action recognition and video alignment.

This work features several extensions to our conference publication [65], which focused on embedding fully visible 2D poses. First, we extend our framework to handle embedding partially-visible 2D poses, which allows our embeddings to be more applicable to in-the-wild cases and enables users to define keypoint subsets for retrieval. We achieve this using a visibility mask and random keypoint dropouts during training, and we investigate the effect of different keypoint dropout distributions. Second, we develop a benchmark for partial keypoint retrieval, for both natural occlusions and targeted pose retrieval, where users can specify retrieval of partial matches to an input 2D pose. Finally, we present a more extensive evaluation of our model and baselines, including comparing to more 3D pose estimation techniques [76, 35] and datasets [43].

Our pose embedding is applicable to fully and partially visible 2D poses without using camera parameters. Our code is released at <https://github.com/google-research/google-research/tree/master/poem>. embeddings to address inherent ambiguities in 2D pose due to 3D-to-2D projection.

2 Related Work

We embed 2D human poses such that embedding space distance corresponds to 3D pose similarity. We provide a review of the relevant literature from representation learning, human pose estimation, and retrieval.

Representation Learning We are working to understand similarity in human poses across views. To capture measures of similarity between inputs, most works generally use contrastive loss [4, 18, 49, 52, 8] or triplet loss (based on tuple ranking) [70, 63, 71, 21]. These losses are used to push together examples that are similar in the embedding space and pull apart examples that are dissimilar. In visual representation learning [49, 52, 8], this similarity generally corresponds to image classes (such as those from ImageNet [11]). Our work is distinct in that our similarity measure is based on 3D pose distance and we embed 2D poses, which allows us to explore new approaches for 2D pose representations.

In our work, we learn a mapping from Euclidean distance in the embedding space to a probabilistic pose similarity score. This probabilistic similarity captures closeness in 3D pose space from 2D poses. Our work is inspired by the mapping used in soft contrastive loss [49] for learning from an occluded N-digit MNIST dataset.

During training of contrastive loss or triplet loss, the number of possible training tuples increases exponentially with respect to the number of samples in the tuple, and not all combinations are equally informative. To find informative training tuples, various mining strategies are proposed [63, 72, 50, 21]. In particular, semi-hard triplet mining has been widely used [63, 72, 55]. We measure the hardness of a negative sample based on its embedding distance to the anchor. Commonly, this distance is the Euclidean distance [70, 71, 63, 21], but any differentiable distance function could be applied [21]. In particular, [24, 27] show that alternative distance metrics also work for image and object retrieval. In our work, the distance metric is based on a probabilistic 3D pose similarity score from embedded 2D poses.

Most of the papers discussed above involve deterministically mapping inputs to point embeddings. We map inputs to probabilistic embeddings, similar to works such as [69, 3, 49]. Probabilistic embeddings have been

used to model specificity of word embeddings [69], uncertainty in graph representations [3], and input uncertainty due to occlusion [49]. We will apply probabilistic embeddings to address inherent ambiguities in 2D pose due to 3D-to-2D projection.

Human Pose Estimation 3D human pose estimation from 2D information, such as images or 2D poses, is a widely explored area [44, 6, 56, 59, 78, 66, 60, 67, 7, 61]. Instead of mapping 2D poses to 3D poses, our work maps 2D poses to a view-invariant embedding space. This embedding space enables detected 2D poses to be matched across views and is directly applicable to pose retrieval, action recognition, and video alignment.

Many approaches work to estimate 3D poses in the camera coordinate system [44, 6, 56, 59, 78, 66, 60, 67, 7, 38, 74]. Since the pose description changes based on camera viewpoint, 3D poses in the camera coordinate frame is not view-invariant and cross-view retrieval requires rigid alignment for every pose pair.

2D-to-3D lifting pose estimators [44, 6, 56, 59, 76] use detected 2D poses as inputs, similar to our approach. Some of these works [38, 74] also use data augmentation to improve generalization to new poses for 3D lifting. Lifting models are trained to regress to 3D pose keypoints, while our model is trained using representation learning and outputs an embedding distribution. In addition, other works use multi-view datasets to predict 3D poses in the global coordinate frame [57, 35, 28, 61, 68]. Our work differs from these methods with our goal of learning view-invariant embeddings, approach of representation learning and downstream tasks.

View Invariance When we capture a 3D scene in 2D as images or videos, changing the viewpoint often does not change other properties of the scene. To the best of our knowledge, we are the first to explore mapping 2D input, as 2D poses, to a view-invariant embedding space through representation learning. View-invariance from 2D information can enable a variety of vision applications, such as motion analysis [31, 30, 62], video alignment [14], tracking [51], vehicle and human re-identification [10, 77], object classification and retrieval [36, 23, 22], and action recognition [58, 40, 73, 37]. These downstream tasks can potentially benefit from our view-invariant pose embeddings. Here, we investigate how view-invariance can be applied to cross-view retrieval, action recognition, and video alignment.

Retrieval With growing amounts of recorded data, retrieval has received increasing amounts of attention in research communities [36, 47, 23, 22, 20]. The ability to retrieve similar images and videos according to different

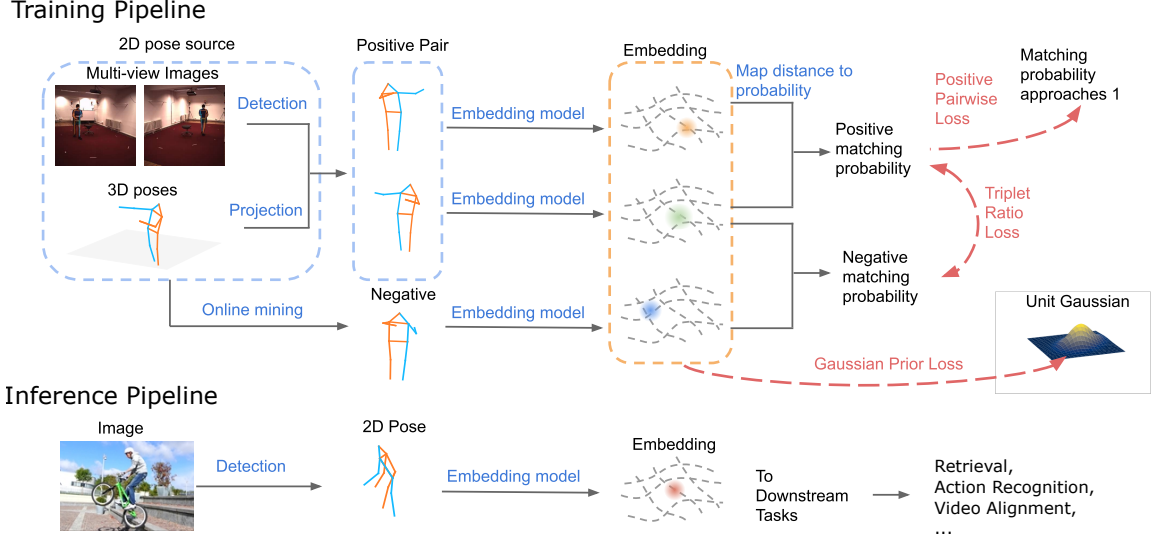


Fig. 2: Overview of Pr-UIPE model training and inference. Our model takes keypoint input from a single 2D pose (detected from images and/or projected from 3D poses) and predicts embedding distributions. Three losses are applied during training.

similarity metrics is useful for a variety of vision applications. Here, we would like to retrieve images containing similar 3D poses using 2D information. We show that this ability also enables us to achieve cross view action recognition and video alignment.

Pose retrieval of 2D poses in the same view has been studied by [47]. This method embeds images with similar 2D poses in the same view close together, and so is not view-invariant. Our method focuses on learning view-invariance, and we also differ from [47] in method, using probabilistic 2D pose embeddings.

Compared to classification-based retrieval tasks, such as object retrieval [22], our domain differs in a few ways. Our labels are continuous 3D poses, whereas in object recognition tasks, each embedding is associated with a discrete class label. Furthermore, we embed 2D poses instead of images. Our approach allows us to investigate the impact of input 2D uncertainty with probabilistic embeddings and explore different methods to measure cross-view pose retrieval confidence. We hope that our work provides a novel perspective on view invariance for human poses.

3 View-Invariant Probabilistic Pose Embedding

Our goal is to embed 2D poses such that distances in the embedding space correspond to similarities of their corresponding absolute 3D poses in Euclidean space. We achieve this view invariance property through our triplet ratio loss (Section 3.2), which pushes together

2D poses corresponding to similar 3D poses and pulls apart 2D poses corresponding to dissimilar 3D poses. The positive pairwise loss (Section 3.3) is applied to increase the matching probability of similar poses. Finally, the Gaussian prior loss (Section 3.4) helps regularize embedding magnitude and variance. The training and inference framework of our model is illustrated in Fig. 2.

3.1 Matching Definition

We define a measure of similarity so that we can push together 2D poses corresponding to similar 3D poses. The 3D pose space is continuous, and two 3D poses can be trivially different without being identical. To account for this, we define two 3D poses to be matching if they are visually similar regardless of viewpoint. Given two sets of 3D keypoints $(\mathbf{y}_i, \mathbf{y}_j)$, we define a matching indicator function

$$m_{ij} = \begin{cases} 1, & \text{if NP-MPJPE}(\mathbf{y}_i, \mathbf{y}_j) \leq \kappa \\ 0, & \text{otherwise,} \end{cases} \quad (1)$$

where κ controls visual similarity between matching poses. Here, we use mean per joint position error (MPJPE) [25] between the two sets of 3D pose keypoints as a proxy to quantify their visual similarity. Before computing MPJPE, we normalize the 3D poses, as described in Section 3.6, and apply Procrustes alignment between them. We do this in order for our model to be view-invariant and to disregard rotation, translation, or scale

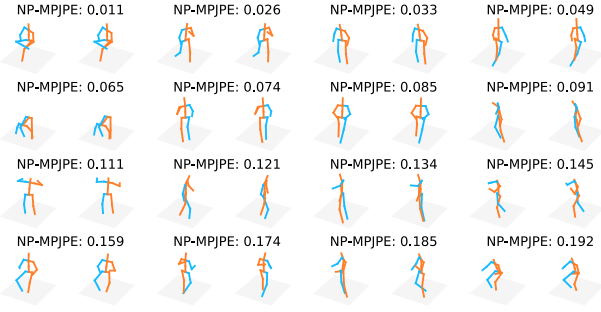


Fig. 3: 3D pose pairs with different NP-MPJPE, where the NP-MPJPE increases with each row. The poses are randomly sampled from the hold-out set of H3.6M. Row 1 shows pairs with 0.00 to 0.05 NP-MPJPE, row 2 shows pairs with 0.05 to 0.10 NP-MPJPE, row 3 shows pairs with 0.10 to 0.15 NP-MPJPE, and row 4 shows pairs with 0.15 to 0.20 NP-MPJPE.

differences between 3D poses. We refer to this normalized, Procrustes aligned MPJPE as **NP-MPJPE**.

Fig. 3 demonstrates sampled 3D pose pairs with different ranges of corresponding NP-MPJPE between them. This plot shows the effect of choosing different κ , which controls matching threshold between 3D poses. Unless stated otherwise, our models use $\kappa = 0.10$, which corresponds to using the first two rows as matching pairs and the rest of the rows as non-matching. We note that pairs in rows 3 and 4 shows significant visual differences as compared with the first two rows. In general, κ can be set by the user based on the perception of visual similarity.

3.2 Triplet Ratio Loss

The triplet ratio loss aims to embed 2D poses based on the matching indicator function (1). Let n be the dimension of the input 2D pose keypoints \mathbf{x} , and d be the dimension of the output embedding. We would like to learn a mapping $f: \mathbb{R}^n \rightarrow \mathbb{R}^d$, such that:

$$D(\mathbf{z}_i, \mathbf{z}_j) < D(\mathbf{z}_i, \mathbf{z}_{j'}), \forall m_{ij} > m_{ij'}, \quad (2)$$

where $\mathbf{z} = f(\mathbf{x})$, and $D(\mathbf{z}_i, \mathbf{z}_j)$ is an embedding space distance measure.

For a pair of input 2D poses $(\mathbf{x}_i, \mathbf{x}_j)$, we define $p(m|\mathbf{x}_i, \mathbf{x}_j)$ to be the probability that their corresponding 3D poses $(\mathbf{y}_i, \mathbf{y}_j)$ match, that is, they are visually similar. While it is difficult to define this probability directly, we propose to assign its values by estimating $p(m|\mathbf{z}_i, \mathbf{z}_j)$ via metric learning. We know that if two 3D poses are identical, then $p(m|\mathbf{x}_i, \mathbf{x}_j) = 1$, and if two 3D poses are sufficiently different, $p(m|\mathbf{x}_i, \mathbf{x}_j)$ should be

small. For any given input triplet $(\mathbf{x}_i, \mathbf{x}_{i+}, \mathbf{x}_{i-})$ with $m_{i,i+} > m_{i,i-}$, we want

$$\frac{p(m|\mathbf{z}_i, \mathbf{z}_{i+})}{p(m|\mathbf{z}_i, \mathbf{z}_{i-})} \geq \beta, \quad (3)$$

where $\beta > 1$ represents the ratio of the matching probability of a similar 3D pose pair to that of a dissimilar pair. That is, the matching probability of a positive pair should be larger than the matching probability of negative pair.

Applying negative logarithm to both sides, we have

$$(-\log p(m|\mathbf{z}_i, \mathbf{z}_{i+})) - (-\log p(m|\mathbf{z}_i, \mathbf{z}_{i-})) \leq -\log \beta. \quad (4)$$

We note that the training can optimize this using the triplet loss framework [63]. Given batch size N , we define triplet ratio loss $\mathcal{L}_{\text{ratio}}$ as

$$\mathcal{L}_{\text{ratio}} = \sum_{i=1}^N \max(0, D_m(\mathbf{z}_i, \mathbf{z}_{i+}) - D_m(\mathbf{z}_i, \mathbf{z}_{i-}) + \alpha), \quad (5)$$

with distance kernel $D_m(\mathbf{z}_i, \mathbf{z}_j) = -\log p(m|\mathbf{z}_i, \mathbf{z}_j)$ and margin $\alpha = \log \beta$. To form a triplet $(\mathbf{x}_i, \mathbf{x}_{i+}, \mathbf{x}_{i-})$, we set the anchor \mathbf{x}_i and positive \mathbf{x}_{i+} to be projected from the same 3D pose and perform online semi-hard negative mining [63] to find \mathbf{x}_{i-} .

We can compute the matching probability using our embeddings. To compute $p(m|\mathbf{z}_i, \mathbf{z}_j)$, we use the formulation proposed by [49]:

$$p(m|\mathbf{z}_i, \mathbf{z}_j) = \sigma(-a\|\mathbf{z}_i - \mathbf{z}_j\|_2 + b), \quad (6)$$

where σ is a sigmoid function, and the trainable scalar parameters $a > 0$ and $b \in \mathbb{R}$ calibrate embedding distances to probabilistic similarity.

3.3 Positive Pairwise Loss

Since the positive pairs in our triplets have identical 3D poses, we would like them to have high matching probabilities. We encourage this property by adding the positive pairwise loss

$$\mathcal{L}_{\text{positive}} = \sum_{i=1}^N -\log p(m|\mathbf{z}_i, \mathbf{z}_{i+}). \quad (7)$$

The combination of $\mathcal{L}_{\text{ratio}}$ and $\mathcal{L}_{\text{positive}}$ can be applied to training point embedding models, which we refer to as VIPE.

3.4 Probabilistic Embeddings

In this section, we discuss the extension of VIPE to the probabilistic formulation Pr-VIPE. The inputs to our model, 2D pose keypoints, are inherently ambiguous, and there are many valid 3D poses that can be projected to a similar 2D pose [1]. This input uncertainty can be difficult to model using point embeddings [32,49]. We investigate representing this uncertainty using distributions in the embedding space by mapping 2D poses to probabilistic embeddings: $\mathbf{x} \rightarrow p(\mathbf{z}|\mathbf{x})$. Similar to [49], we extend the input matching probability (6) to using probabilistic embeddings as $p(m|\mathbf{x}_i, \mathbf{x}_j) = \int p(m|\mathbf{z}_i, \mathbf{z}_j)p(\mathbf{z}_i|\mathbf{x}_i)p(\mathbf{z}_j|\mathbf{x}_j)d\mathbf{z}_i d\mathbf{z}_j$, which can be approximated using Monte-Carlo sampling with K samples drawn from each distribution as

$$p(m|\mathbf{x}_i, \mathbf{x}_j) \approx \frac{1}{K^2} \sum_{k_1=1}^K \sum_{k_2=1}^K p(m|\mathbf{z}_i^{(k_1)}, \mathbf{z}_j^{(k_2)}). \quad (8)$$

We model $p(\mathbf{z}|\mathbf{x})$ as a d -dimensional Gaussian with a diagonal covariance matrix. The model outputs mean $\mu(\mathbf{x}) \in \mathbb{R}^d$ and covariance $\Sigma(\mathbf{x}) \in \mathbb{R}^d$ with a shared base network and separate output layers. During sampling, we use the reparameterization trick [33], by first sampling from a unit Gaussian $\epsilon^{(k)} \sim \mathcal{N}(\mathbf{0}, \mathbf{I})$ and then computing $\mathbf{z}^{(k)} = \mu(\mathbf{x}) + \epsilon^{(k)} \cdot \text{diag}(\Sigma(\mathbf{x})^{1/2})$ during training for easy backpropagation.

We place a unit Gaussian prior on our embeddings with KL divergence by adding the Gaussian prior loss

$$\mathcal{L}_{\text{prior}} = \sum_{i=1}^N D_{\text{KL}}(\mathcal{N}(\mu(\mathbf{x}_i), \Sigma(\mathbf{x}_i)) \parallel \mathcal{N}(\mathbf{0}, \mathbf{I})). \quad (9)$$

This loss prevents variance from collapsing to zero and regularizes embedding mean magnitudes

3.5 Training Objective

Our full training objective for Pr-VIPE is:

$$\mathcal{L} = \mathcal{L}_{\text{ratio}} + \gamma_1 \mathcal{L}_{\text{positive}} + \gamma_2 \mathcal{L}_{\text{prior}}. \quad (10)$$

We optimize training with respect to a and b in (6) and the embedding function. We set γ_1 and γ_2 such that all the terms are approximately the same magnitude.

3.6 Pose Normalization

We normalize our 2D and 3D poses such that camera parameters are not needed during training and inference. For 3D poses, our normalization procedure is similar to that in [7]. We translate a 3D pose so that the

pelvis located at the origin. We then scale the pelvis to spine to neck distance to a unit scale. For 2D poses, we translate the keypoints so that the center between left hip and right hip is at the origin. Then we normalize the pose such that the maximum distance between shoulder and hip joints is 0.5. This maximum distance is computed between all pairwise distances among right shoulder, left shoulder, right hip, and left hip.

3.7 Camera Augmentation

During training, 2D pose triplets consists of detected and/or projected 2D keypoints as shown in Fig. 2. When we train with detected 2D keypoints only, we are constrained to the camera views in training images. To reduce overfitting to these views, we perform camera augmentation by generating triplets using detected keypoints alongside projected 2D keypoints at random views.

To form triplets using multi-view image pairs, we use detected 2D keypoints from different views as anchor-positive pairs. To use projected 2D keypoints, we perform two random rotations to a normalized input 3D pose to generate two 2D poses from different views for anchor-positive pairs. Camera augmentation is then performed by using a mixture of detected and projected 2D keypoints.

3.8 Inference

At inference time, our model takes a single 2D pose (either from detection or projection) and outputs the mean and the variance of the embedding Gaussian distribution. We do not need explicit camera parameters for training or inference.

4 Occlusion-Robust Pose Embedding

In this section, we extend the Pr-VIPE framework to explicitly handle inputs with different keypoint visibilities by embedding them into a single space using a single model. We first present our keypoint visibility representation for modeling in Section 4.1. We then propose to study two keypoint occlusion augmentation strategies in Section 4.2: independent keypoint dropout and structured keypoint dropout. Finally, we describe training with keypoint occlusions in Section 4.3.

4.1 Keypoint Visibility Representation

We use a binary mask vector \mathbf{v} to represent the visibility of each keypoint for a 2D pose \mathbf{x} , where each entry

of \mathbf{v} is 1 if its corresponding keypoint is visible and 0 otherwise. This keypoint visibility indicator can represent whether a keypoint is not visible due to occlusion or whether a keypoint is masked as excluded. For example, keypoint masks can be used for retrieval of partial pose matches. When a keypoint has mask 0, its normalized coordinates are also set to 0. We concatenate the keypoint mask with normalized 2D keypoints as the model input.

In practice, we always consider the torso keypoints (two shoulders and two hips) as visible, based on the fact that torso has a near-rigid shape represented by these four keypoints, for which our 2D keypoint detector mostly gives reliable estimates about their locations.

4.2 Keypoint Occlusion Augmentation

In order to enable the model to be robust to partially visible pose keypoints, we generate various patterns of keypoint occlusion during training. It is ideal to train our model on various realistic keypoint occlusion patterns. However, datasets in practice may not contain diverse occlusion patterns, so we address this by synthesizing occlusion patterns and using the synthesized patterns for training. Here, we explore two methods for creating synthetic keypoint visibility masks:

Independent Keypoint Dropout One simple way to synthesize keypoint occlusion patterns is to randomly mask keypoints during training. We apply an i.i.d. sampling with fixed chance q to determine whether each keypoint of an input 2D pose is to be marked as unavailable at each training iteration.

Structured Keypoint Dropout In realistic photos, the visibilities of pose keypoints are usually not i.i.d. Therefore, a more sophisticated way to synthesize “realistic” keypoint occlusion patterns is to consider the joint distribution of keypoint visibilities. We estimate 2D keypoints of about 300 million pose samples detected from random in-the-wild photos. We binarize the keypoint detection confidence via thresholding and use it as a proxy to keypoint visibility. We then approximate the joint distribution of keypoint visibility patterns in the wild with its counting frequency.

The number of patterns in the joint distribution is exponential to the number of keypoints. We decompose the full body pose graph (keypoint definition in Appendix A) into 6 cliques:

- Head: nose tip.
- Torso: left shoulder, right shoulder, left hip, right hip.

- Left arm/torso: left wrist, left elbow, left shoulder, left hip.
- Right arm/torso: right wrist, right elbow, right shoulder, right hip.
- Upper legs: left hip, right hip, left knee, right knee.
- Lower legs: left knee, right knee, left ankle, right ankle.

We sample each clique following this order. When sampling a clique, if some of its keypoints have been assigned a visibility mask value, then we marginalize them out from the joint distribution, and sample from the rest. All of the cliques have at most four keypoints, and thus marginalizing and sampling from their joint distributions can be easily handled.

In practice during training, we first apply a threshold to keypoint detection confidence and mask keypoints with low confidence. Then we further sample the keypoint mask based on either strategies.

4.3 Training with Occlusions

Following the Pr-UIPE triplet training framework, we generate keypoint visibility mask using the strategies mentioned above for all anchor poses and use fully visibility masks for their positive matches. Semi-hard negative matches are mined online from the batch, and the negative labels are determined according to the 3D pose matching definition (Section 3.1) between a subset of visible keypoints to their corresponding anchor poses.

5 Experiments

In this section, we describe our experimental procedures and present our model evaluations on three tasks: cross-view retrieval, action recognition, and video alignment. First, we show our model performance on pose retrieval across different camera views for fully-visible poses (Section 5.3) and partially-visible poses (Section 5.4). Second, we show that our embeddings can be directly applied to action recognition (Section 5.5), without any additional training. Finally, we present results of our embeddings for video alignment (Section 5.6).

5.1 Datasets

For all the experiments in this paper, we only train on a subset of the Human3.6M [25] dataset. For pose retrieval experiments, we validate on the Human3.6M hold-out set and test on a different dataset MPI-INF-3DHP [45], which is unseen during training and free

from parameter tuning. To evaluate models for handling partially visible poses, we create a number of datasets based on the Human3.6M hold-out set with synthetically occluded keypoints. Additionally, we use the 3D Poses in the Wild dataset [43], which includes realistic keypoint occlusions. We present qualitative results on MPII Human Pose [2], for which 3D groundtruth is not available. For action recognition and video alignment experiments, we apply our model on Penn Action [75], a video action dataset unseen during training.

Human3.6M (H3.6M) [25] H3.6M is a large human pose dataset recorded from 4 chest-level cameras with 3D pose groundtruth. We follow the standard protocol [44]: train on Subject 1, 5, 6, 7, and 8, and hold out Subject 9 and 11 for validation. For evaluation, we remove near-duplicate 3D poses within 0.02 NP-MPJPE, resulting in a total of 10910 evaluation frames per camera. This process is camera-consistent, meaning if a frame is selected under one camera, it is selected under all cameras, so that the perfect retrieval result is possible. Note that H3.6M is the only dataset we use for training our models in this paper.

The following datasets are used **only for testing and not for any training**:

MPI-INF-3DHP (3DHP) [45] 3DHP is a more recent human pose dataset that contains 14 diverse camera views and scenarios, covering more pose variations than H3.6M [45]. We use 11 cameras from this dataset and exclude the 3 cameras with overhead views. Similar to H3.6M, we remove near-duplicate 3D poses, resulting in 6824 frames per camera. We use all 8 subjects from the train split of 3DHP.

3D Poses in the Wild (3DPW) [43] 3DPW contains 60 videos of human poses captured in the wild with realistic occlusions. We use this dataset to evaluate our occlusion-robust models and related baselines in terms of pose retrieval. We split the test set originally proposed in [43] by randomly selecting 45% of the video sequences for query samples, and the rest for index samples. We evenly downsample the video frames by 2, and only include a query sample if (1) its four 2D torso keypoints (left shoulder, right shoulder, left hip, right hip) are available, and (2) there exists at least one sample in the index set whose 3D pose is less than 0.1 NP-MPJPE apart. Due to the randomness in splitting query/index videos, we sample 5 splits and report the averaged results for our experiments on this dataset.

MPII Human Pose (2DHP) [2] This dataset is commonly used in 2D pose estimation, containing about 25K in-the-wild images. Since groundtruth 3D poses are not available, we show qualitative results on this dataset.

Penn Action [75] This dataset contains 2326 trimmed videos for 15 pose-based actions taken from 4 different views. We follow the standard protocol [48] for our action classification and video alignment experiments.

5.2 Implementation Details

Our implementation is in TensorFlow, and all the models are trained with CPUs. The backbone network architecture for our model is based on [44] for simplicity and fair comparison between 3D lifting and embedding. We use two residual blocks, batch normalization, 0.3 dropout, and no weight norm clipping. Unless stated otherwise, we use $d = 32$ as a good trade-off between embedding size and accuracy. To weigh different losses, we use $w_{\text{ratio}} = 1$, $w_{\text{positive}} = 0.005$, and $w_{\text{prior}} = 0.001$. We choose $\beta = 2$ for the triplet ratio loss margin and $K = 20$ for the number of samples. During training, we normalize matching probabilities to within $[0.05, 0.95]$ for numerical stability. The matching NP-MPJPE threshold is $\kappa = 0.1$ for all training and evaluation. Ablation studies on hyperparameters can be found in Section 5.8.

We use PersonLab [53] 2D keypoint detector for our experiments, unless stated otherwise, but our approach does not rely on a particular 2D keypoint detector. For random rotation during camera augmentation, we uniformly sample azimuth angle between $\pm 180^\circ$, elevation between $\pm 30^\circ$, and roll between $\pm 30^\circ$. We use Adam optimizer [13] with fixed learning rate 0.02, and batch size $N = 256$. Our batch consists of an even mix of detected and projected 2D keypoints, which includes anchor and positive pairs from different sources. For the occlusion-robust model training, we evenly mix triplets all fully visible poses and triplets with partial visible poses in a batch.

5.3 Cross-View Pose Retrieval

The goal of cross-view pose retrieval is to retrieve matching 2D poses from different camera views given a 2D pose from one view. This task is evaluated using multi-view human pose datasets, since we are able to have 2D pose detections of the same 3D pose across views. In this evaluation, we query using detected 2D keypoints from one camera view and find the nearest neighbors

Table 1: Comparison of cross-view pose retrieval results Hit@ k (%) on H3.6M and 3DHP. * indicates normalization and Procrustes alignment are required to compare query-index pairs.

Dataset k	H3.6M				3DHP (Chest)				3DHP (All)			
	1	5	10	20	1	5	10	20	1	5	10	20
2D keypoints*	27.4	41.4	45.8	49.7	5.75	11.2	12.1	18.5	10.3	18.7	22.6	26.5
3D lifting*	68.8	85.4	89.5	92.5	26.0	47.1	55.9	63.8	25.5	45.9	54.6	62.7
<i>L2</i> -VIPE	73.5	89.7	93.2	95.5	25.8	46.6	55.1	62.8	21.3	39.3	47.4	55.0
<i>L2</i> -VIPE (w/ aug.)	72.3	89.2	92.9	95.3	28.5	50.7	59.5	67.4	27.4	48.4	57.2	65.0
Pr-VIPE	77.9	93.3	95.4	98.2	28.5	52.7	63.2	72.8	22.7	43.1	52.6	62.1
Pr-VIPE (w/ aug.)	75.1	91.6	95.0	97.3	30.0	54.8	64.9	74.1	28.3	51.2	61.2	70.4

Table 2: Comparison with recent methods of cross-view pose retrieval results Hit@ k (%) on H3.6M. * indicates normalization and Procrustes alignment are required to compare query-index pairs.

Model	H3.6M			
	$k = 1$	$k = 5$	$k = 10$	$k = 20$
3D lifting*	68.1	85.5	90.0	93.4
SemGCN*	70.7	88.4	92.3	95.1
EpipolarPose*	78.0	92.2	95.2	97.1
Pr-VIPE	81.6	95.4	97.9	99.1

in the embedding space from a different camera view. We iterate through all camera pairs in the dataset as query and index. Results averaged across all cameras pairs are reported.

5.3.1 Evaluation Procedure

We report Hit@ k with $k = 1, 5, 10$, and 20 on pose retrievals, which is the percentage of top- k retrieved poses that have at least one accurate retrieval. A retrieval is considered accurate if the 3D groundtruth from the retrieved pose satisfies the matching function (1) with $\kappa = 0.1$.

On H3.6M and 3DHP, we compare Pr-VIPE with using 2D pose inputs, 2D-to-3D lifting models [44] and *L2*-VIPE. *L2*-VIPE outputs *L2*-normalized point embeddings, and is trained with the squared *L2* distance kernel, similar to [63]. For fair comparison, we use the same backbone network architecture for all the models. Notably, this architecture [44] has been tuned for lifting tasks on H3.6M. Since the estimated 3D poses in camera coordinates are not view-invariant, we apply normalization and Procrustes alignment to align the estimated 3D poses between index and query for retrieval. In comparison, our embeddings do not require any alignment or other post-processing during retrieval.

On H3.6M, we further compare with two state-of-the-art 3D lifting methods: Semantic Graph Convolutional Networks (SemGCN) [76] and EpipolarPose [35].

SemGCN leverages graph convolutional networks [34] to encode 2D poses with a skeleton-based graph representation. We train SemGCN on 2D poses from a Cascaded Pyramid Network (CPN) [9] pose detector, which takes bounding boxes detected by Mask R-CNN [19] as inputs. Following [56], the CPN model is pre-trained on COCO [39] and then fine-tuned on H3.6M. EpipolarPose is an image-based 3D pose estimation model. We report the results from its fully supervised version.

For Pr-VIPE, we retrieve poses using nearest neighbors in the embedding space with respect to the sampled matching probability (8), which we refer to as retrieval confidence.

We applied similar camera augmentation to the lifting model, but did not see improvement in performance.

5.3.2 Quantitative Results

From Table 1, we see that Pr-VIPE (with camera augmentation) outperforms all baselines for H3.6M and 3DHP. The H3.6M results shown are on the hold-out set, and 3DHP is unseen during training. The first row in Table 1 shows retrieval accuracy using aligned 2D poses. The poor performance of using input 2D keypoints for retrieval from different views confirms the fact that models must learn view invariance from inputs for this task.

When we use all cameras from 3DHP, we evaluate the generalization ability of models to new poses and new views. When we evaluate using only the 5 chest-level cameras from 3DHP, the views are more similar to the training set in H3.6M. This enables us to mainly evaluate for generalization to new poses.

Table 1 shows that Pr-VIPE without camera augmentation is able to perform better than the baselines for H3.6M and 3DHP (chest-level cameras). This result shows that Pr-VIPE is able to generalize as well as other baseline methods to new poses.

Using Pr-VIPE with camera augmentation improves the performance of Pr-VIPE on 3DHP for both chest-

level cameras and all cameras. This observation indicates that camera augmentation improves model generalization to new views. The same results can be observed for *L2*-VIPE for chest-level and all cameras. We note that 3D lifting models can generalize relatively well to new views with the help of additional Procrustes alignment, which requires expensive SVD computation between every index-query pair. On H3.6M, camera augmentation reduces accuracy slightly for both Pr-VIPE and *L2*-VIPE. This result is likely because camera augmentation reduces overfitting to the training camera views. By performing camera augmentation, Pr-VIPE is able to generalize better to new poses and new views. We note that camera augmentation does not require camera parameters or additional groundtruth.

Table 2 contains comparisons of Pr-VIPE to additional 3D lifting baselines. For this comparison, we follow the standard protocol of 3D pose estimation [35, 76] and evaluate on every 64th frame of H3.6M hold-out set for which the authors provided bounding box data. Table 2 demonstrates that Pr-VIPE, without the need for Procrustes alignment, is able to retrieve poses across views more accurately compared to 3D pose estimation models.

5.3.3 Qualitative Results

Fig. 4 shows qualitative retrieval results using Pr-VIPE (with camera augmentation). As shown in the first and second rows, the retrieval confidence of the model is generally high for H3.6M. This indicates that the retrieved poses are close to their queries in the embedding space. In the third and fourth rows, the retrieval confidence is generally lower for 3DHP compared to H3.6M. This is likely because there are new poses and views unseen during training, which results in the nearest neighbor being slightly further away in the embedding space. We see that the model can generalize to new views as the images are taken at different camera elevations from H3.6M. The rightmost pair on row 4 shows an example of a large NP-MPJPE error due to mis-detection of the legs in the query and index poses.

We show qualitative results using queries from the H3.6M hold-out set to retrieve from 2DHP in the last three rows of Fig. 4. The results on these in-the-wild images indicate that as long as the 2D keypoint detector works reliably, our model is able to retrieve poses across views and subjects.

5.4 Partially-Visible Pose Retrieval

In this section, we evaluate our occlusion-robust embedding for cross-view retrieval of partial 2D poses on

H3.6M and 3DPW. We use the outdoor 3DPW dataset to test our embedding performance on realistic occlusions. Since there are limited realistic occlusions in H3.6M, we synthetically occlude certain keypoints and create two types of test sets for evaluation, namely targeted occlusion and real-distribution occlusion. The targeted occlusion set consists of 10 hand-picked visibility patterns and aims at testing model performance in targeted partial pose search. The real-distribution occlusion consists of the top-50 most common visibility patterns in the wild and aims at testing models' potential performance on random photos in the wild. More details will be introduced next in Section 5.4.1. For all the experiments in this section, we adopt the Pr-VIPE with camera augmentation (Section 3) setting, and apply different keypoint occlusion augmentation strategies (Section 4.2) during training.

5.4.1 Evaluation Procedure

Our evaluation procedure is similar to the full body retrieval procedure above in Section 5.3.1. We report retrieval performance with Hit@ k with $k = 1, 5, 10$, and 20 and a retrieval is considered accurate if the retrieved 3D groundtruth satisfies the matching function (1) with $\kappa = 0.1$.

On H3.6M, we conduct two types of synthetic tests for model performance with different keypoint visibility patterns:

Targeted Occlusion We define 10 visibility patterns, including missing left or right or both arms, missing left or right or both legs, and missing one arm and one leg, as the targeted occlusions. For each pattern, we create a pair of query/index sets, such that all the query samples have the designated visibility pattern, while all the index samples always have full visibility. We evaluate models on these 10 sets and report the averaged results.

We compare the two proposed keypoint occlusion augmentation training strategies, i.e., independent keypoint dropout and structured keypoint dropout, along with two other baselines, one ("None") that uses uniform (all-one) visibility masks and one ("Thresholding") that uses visibility masks only from thresholding keypoint detection confidence during training. To demonstrate the upper-bound performance for reference, we further train 10 models with fixed visibility input, each dedicated to one of the 10 targeted occlusion patterns. Each individual model is evaluated on its dedicated visibility pattern.

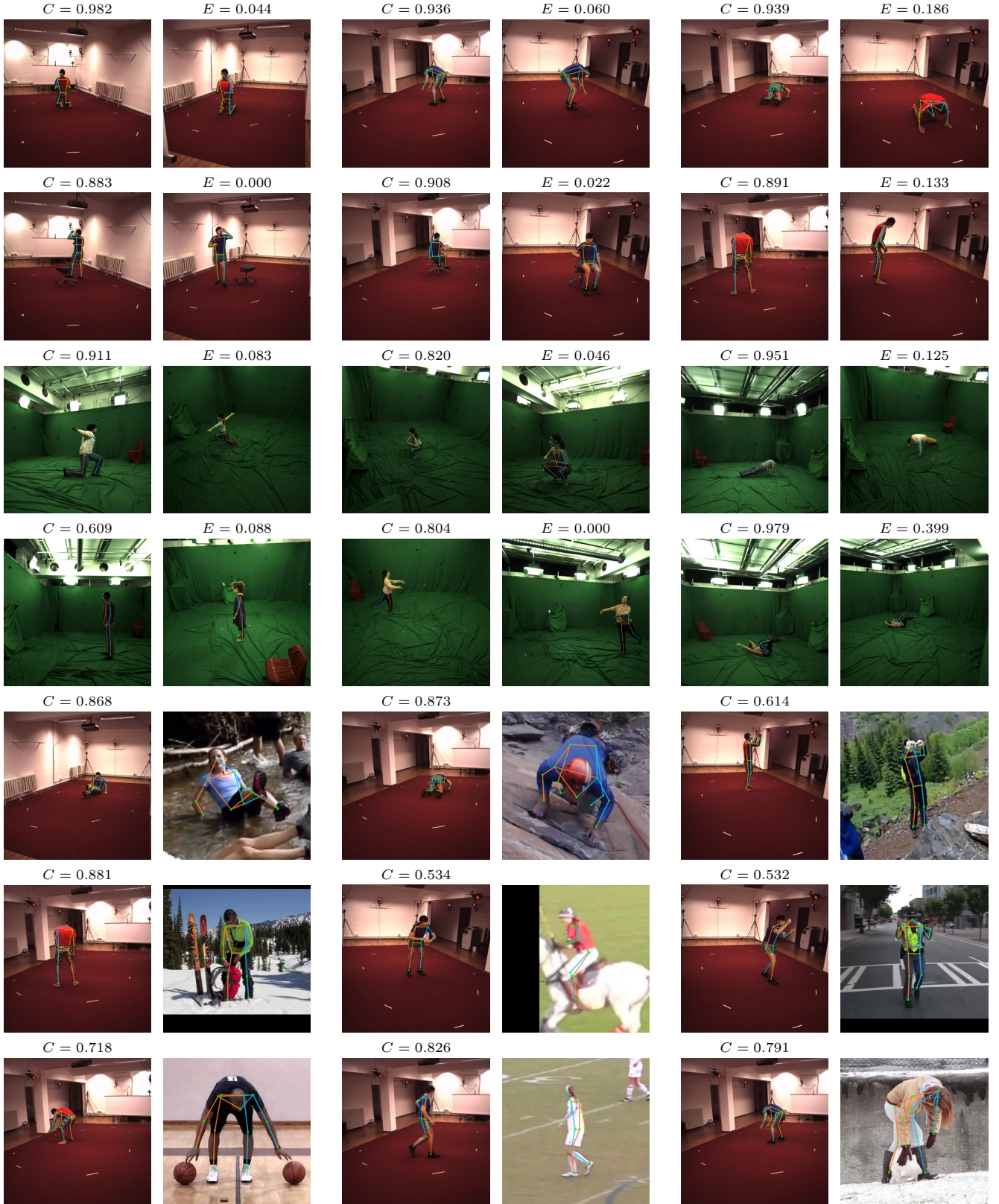


Fig. 4: Visualization of pose retrieval results. The first and second row are from H3.6M; the third and fourth row are from 3DHP; the last three rows are using queries from H3.6M to retrieve from 2DHP. On each row, we show the query pose on the left for each image pair and the top-1 retrieval using the Pr-UIPE model (w/ aug.) on the right. We display retrieval confidences (“ C ”) and top-1 NP-MPJPEs (“ E ”, if 3D pose groundtruth is available).

Table 3: Comparison of cross-view pose retrieval results Hit@ k (%) on H3.6M with synthetic occlusions using different keypoint occlusion augmentation training strategies. [†] indicates the results are from dedicated models that are trained for each visibility pattern and evaluated with query/index samples with identical keypoint visibilities.

Evaluation type	Keypoint dropout	$k = 1$	$k = 5$	$k = 10$	$k = 20$
No occlusion	None	75.1	91.6	95.0	97.3
	Thresholding	73.2	90.6	94.4	96.8
	Independent	74.2	91.1	94.8	97.1
	Structured	74.0	91.1	94.8	97.0
Targeted occlusion	None	3.36	6.04	7.95	10.7
	Thresholding	45.5	69.9	77.3	83.2
	Independent	68.7	88.9	93.3	96.1
	Structured	68.6	89.0	93.4	96.1
	Dedicated [†]	76.4	92.1	95.3	97.2
Real-distribution occlusion	None	43.3	55.0	59.1	63.6
	Thresholding	58.1	80.6	87.0	91.7
	Independent	72.1	90.7	94.5	97.0
	Structured	72.6	91.0	94.7	97.0

Table 4: Comparison of cross-view pose retrieval results Hit@ k (%) on 3DPW with realistic occlusions using different keypoint occlusion augmentation training strategies.

Keypoint dropout	$k = 1$	$k = 5$	$k = 10$	$k = 20$
None	43.4	61.7	69.6	76.7
Thresholding	62.6	84.9	91.4	95.2
Independent	67.9	89.2	94.2	96.8
Structured	66.5	88.1	93.4	96.4

Real-Distribution Occlusion We test model performance with the top-50 most frequent visibility patterns from the in-the-wild pose keypoint joint distribution introduced in Section 4.2, which accumulatively covers about 96% of the visibility patterns of the 300 million poses. For each pattern, we create a pair of query/index sets, such that all the query samples have the designated visibility pattern. For every index sample, we randomly draw a visibility pattern from the joint distribution whose visible keypoints make a superset of the query visible keypoints. We evaluate models on these 50 sets and report the average results weighted by the frequency of each visibility pattern. It is also worth mentioning that only 5 of the 10 targeted occlusion patterns are among the top-50 in-the-wild patterns.

3DPW provides realistic occlusions on 2D keypoints, which we directly use for masking our model input. We also smear these occlusions to 3D keypoints and only use visible 3D keypoints for NP-MPJPE computation during evaluation.

Using these datasets, we explore Pr-UIPE performance with different keypoint occlusion augmentation strategies described in Section 4.

5.4.2 Quantitative Results

Table 3 shows pose retrieval results on H3.6M synthetic test sets. We see that when training without considering occlusions (“None”), the model performance is significantly lowered when occlusions exist at test time, compared to when no occlusions exist. Relying on limited realistic occlusions from the training set (“Thresholding”) can boost models’ robustness to occlusions as compared to without. The proposed independent or the structured keypoint dropout strategy further provides significant performance improvement under different occlusion scenarios, with only slightly lower performance on fully visible retrieval. Similarly in Table 4, we see that using our proposed keypoint dropout strategies outperform baseline methods by a large margin. The results on the outdoor 3DPW dataset also suggest that our occlusion-robust Pr-UIPE model works in the wild.

For targeted occlusions, the proposed one-for-all models using independent or structured keypoint dropout achieve strong performance compared with the dedicated model upper bounds on several retrieval metrics. Though there is a performance difference between one-for-all models and dedicated models, it is important to note that each dedicated model is limited only to one specific visibility pattern and not robust to other occlusion patterns. In practice, it is infeasible to train and deploy a model for every possible visibility pattern.

For real-distribution occlusions, we observe that using structured dropout outperforms independent dropout with real-distribution occlusions. From a modeling perspective, structured dropout is more flexible than independent dropout at incorporating underlying occlusion pattern statistics into training, and thus has better performance on similarly distributed test time patterns.

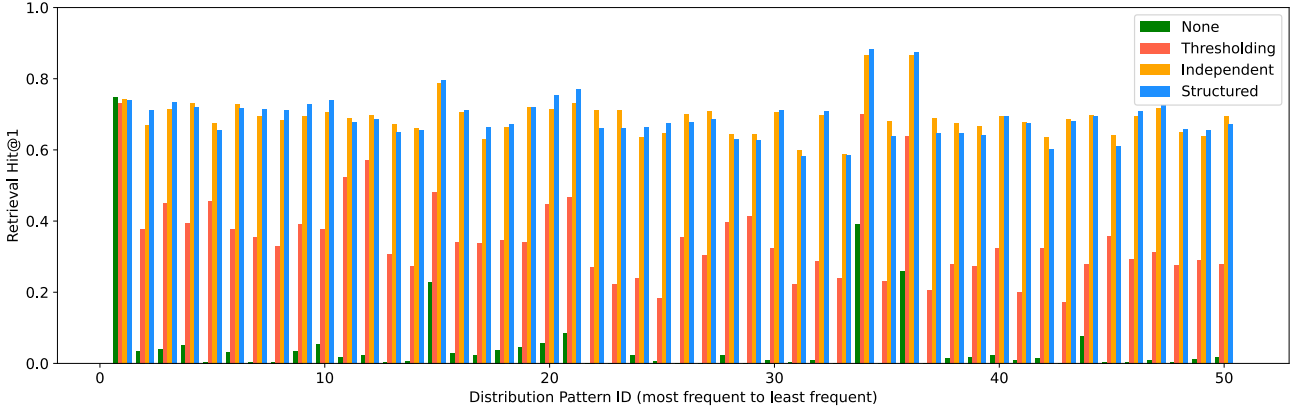


Fig. 5: Comparison of cross-view pose retrieval results Hit@1 for the top-50 most common in-the-wild occlusion patterns using different keypoint dropout methods with Pr-UIPE.

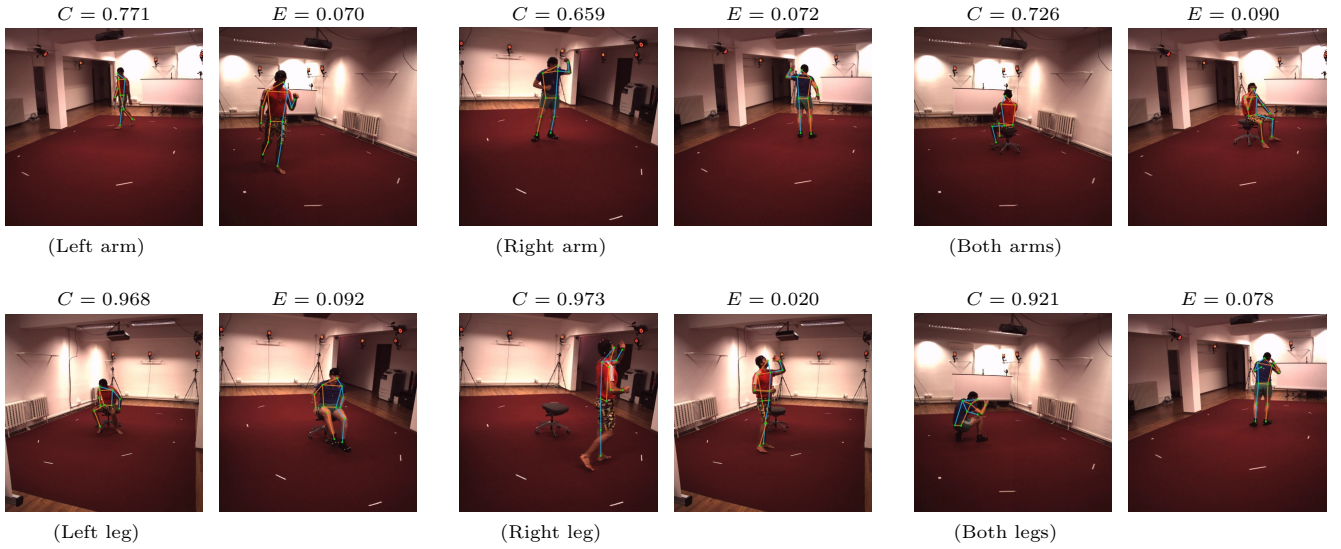


Fig. 6: Visualization of keypoint subset pose retrieval. For each pose pair, we show the query pose on the left and the top-1 retrieval using the Pr-UIPE model (with camera augmentation) on the right. The occluded body parts, synthesized with targeted occlusion patterns, are described under each query images. Only visible keypoints are visualized with the skeletons. Retrieval confidences (“ C ”) and top-1 3D NP-MPJPEs (“ E ”) are also displayed for each retrieval.

Fig. 5 further shows the retrieval results for each of the top-50 most common in-the-wild visibility patterns. We see that on the fully visible pose represented by the first bar, all the dropout methods are similar in performance. As we introduce different occlusion patterns, independent and structured dropout performs much better than the other baselines. In conclusion, training with keypoint occlusion augmentation is important to improving model robustness to partial visibilities.

5.4.3 Qualitative Results

Fig. 6 shows qualitative retrieval results on 6 targeted occlusion patterns using Pr-UIPE (with camera augmentation) trained with structured keypoint dropout. The queries in the top row have left, right, and both arms occluded, respectively. The queries in the bottom row have left, right, and both legs occluded. Using our embeddings, we are able to accurately retrieve poses from the visible keypoint subset. For example, in the bottom right pair, given the visible keypoint subset as the upper body, the top-1 retrieval returns a pose with

Table 5: Comparison of action recognition results on Penn Action.

Methods	RGB	Input Flow	Pose	Accuracy (%)
Nie <i>et al.</i> [48]	✓		✓	85.5
Iqbal <i>et al.</i> [26]			✓	79.0
Cao <i>et al.</i> [5]		✓	✓	95.3
	✓	✓		98.1
Du <i>et al.</i> [12]	✓	✓	✓	97.4
Liu <i>et al.</i> [41]	✓		✓	91.4
Luvizon <i>et al.</i> [42]	✓		✓	98.7
Ours			✓	97.8
Ours (1-view index)			✓	92.8

the same upper body pose, despite its significant difference in the lower body pose. This evaluation also indicates that using our occlusion-robust embedding, one will be able to specify a subset of query keypoints for targeted partial pose retrieval.

5.5 Action Recognition

Our pose embedding can be directly applied to pose-based downstream tasks using simple algorithms. Here, we compare the performance of Pr-UIPE (**only trained on H3.6M, with no additional training**) on the Penn Action dataset against other approaches specifically trained for action recognition on the target dataset.

5.5.1 Evaluation Procedure

To apply our frame embedding to videos, we compute our Pr-UIPE embedding on single video frames and use the negative logarithm of the matching probability (8) as the distance between two frames. Using this per frame distance, we apply temporal averaging within an atrous kernel of size 7 and rate 3 around the two center frames and use this averaged distance as the frame matching distance in a sequence. Given the matching distance, we use standard dynamic time warping (DTW) algorithm to align two pose sequences by minimizing the sum of frame matching distances. The averaged frame matching distance from the DTW alignment of Pr-UIPE matching distance is used as the distance between two video sequences.

We evaluate our embeddings for action recognition using nearest neighbor search with the sequence distance described above. Provided person bounding boxes in each frame, we estimate 2D pose keypoints using [54]. On Penn Action, we use the standard train/test split [48]. Using all the testing videos as queries, we conduct two experiments: (1) we use all training videos as index to

Table 6: Comparison of video alignment results on Penn Action.

Methods	Kendall’s Tau
SaL [46]	0.6336
TCN [64]	0.7353
TCC [14]	0.7328
TCC + SaL [14]	0.7286
TCC + TCN [14]	0.7672
Ours	0.7575
Ours (same-view only)	0.7674
Ours (different-view only)	0.7664

evaluate overall performance and compare with state-of-the-art methods, and (2) we use training videos only under one view as index and evaluate the effectiveness of our embeddings in terms of view-invariance. For this second experiment, actions with zero or only one sample under the index view are ignored, and accuracy is averaged over different views.

We follow the standard evaluation protocol [73] and remove action “strum guitar” and several videos in which less than one third of the target person is visible. We use the official train/test split and report the averaged per-class accuracy. For the view-invariant action recognition experiments in which the index set only contains videos from a single view, we exclude the actions that have zero or only one sample under a particular view. We take the bounding boxes provided with the dataset and use [54] (ResNet101) for 2D pose keypoint estimation. For frames of which the bounding box is missing, we copy the bounding box from the nearest frame. Finally, since our embedding is chiral, but certain actions can be done with either body side (pitching a baseball with left or right hand), when we compare two frames, we extract our embeddings from both the original and the mirrored version of each frame, and use the minimum distance between all the pairwise combinations as the frame distance.

5.5.2 Results

Table 5 demonstrates that our embeddings can achieve competitive results on pose-based action classification without any training on the target domain or using image context information. Pr-UIPE with nearest neighbor retrieval is able to outperform the existing best baseline that only uses pose input, as well as other methods that has access to input image context or optical flow. This result shows that our embedding is applicable to pose-based action recognition without additional training, using the method described in Section 5.5.1 for pose sequences.

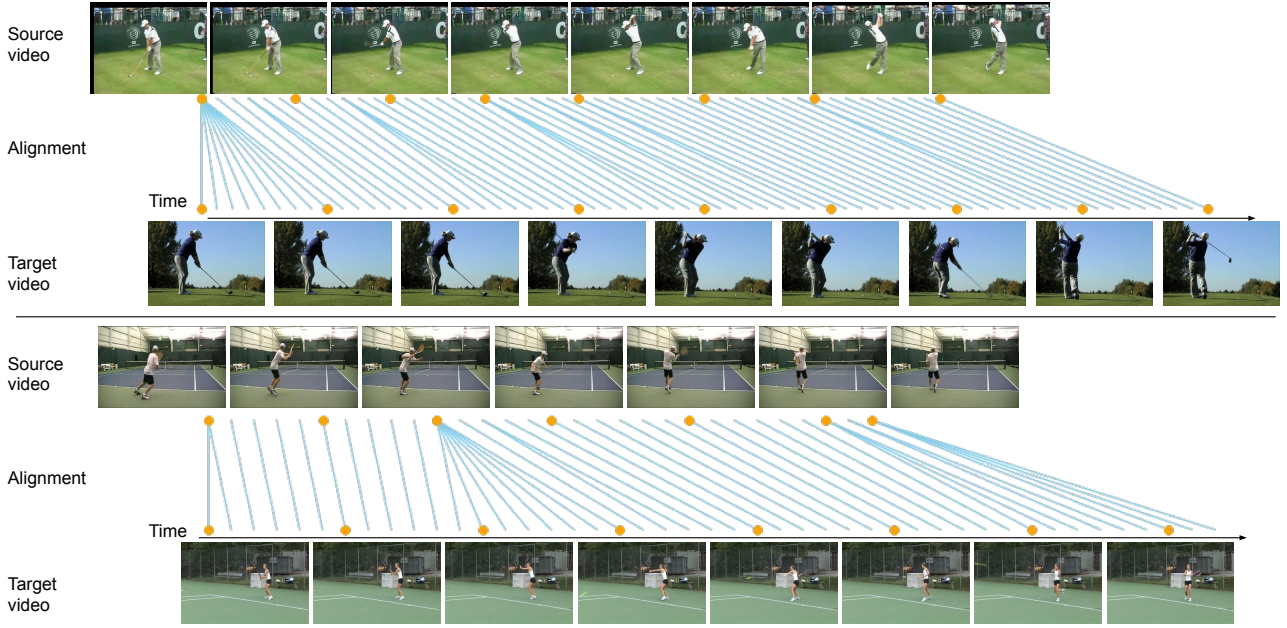


Fig. 7: Video alignment results using Pr-VIPE. The orange dots correspond to the visualized frames, and the blue line segments illustrate the frame alignment.

To evaluate the view-invariance property of our embeddings, we perform action classification using only training videos from a single view. As shown in the last row in Table 5, our embeddings can be used to classify actions from different views using index samples from only one single view with relatively high accuracy. This result further demonstrates the advantages of our view-invariant embeddings.

5.6 Video Alignment

The view-invariance property of Pr-VIPE can be leveraged to align videos with pose sequences across views. We apply Pr-VIPE (**only trained on H3.6M, with no additional training**) on the Penn Action dataset against other approaches specifically trained for video alignment on the target dataset.

5.6.1 Evaluation Procedure

Our embeddings can be used to align human action videos from different views using DTW algorithm. Similar to the temporal embedding stacking described in Section 5.5.1, we apply temporal averaging of the negative log of matching probability within an atrous kernel of size 7 and rate 3 around each frame in a pair of videos. This averaged distance is used as the frame matching distance in a sequence and minimized using dynamic time warping (DTW) to align two pose sequences.

We measure the alignment quality of our embeddings quantitatively using Kendall’s Tau [14], which reflects how well an embedding model can be applied to align unseen sequences if we use nearest neighbor in the embedding space to match frames for video pairs. A value of 1 corresponds to perfect alignment. We also test the view-invariant properties of our embeddings by evaluating Kendall’s Tau on aligning videos pairs from the same view, and aligning pairs with different views.

We follow the protocol in [14], excluding “jump rope” and “strum guitar” from our evaluation. For the evaluations between videos under only the same or different views, we exclude actions that have zero videos under a particular view from the average Kendall’s Tau computation. Since certain actions can be done with either body side, for a video pair (v_1, v_2) , we compute the Kendall’s Taus between (v_1, v_2) and $(v_1, \text{mirror}(v_2))$, and use the larger number.

5.6.2 Results

In Table 6, we compare our results with other video embedding baselines that are trained for the alignment task on Penn Action. Results show that Pr-VIPE performs better than all the method that use a single type of loss. While Pr-VIPE is slightly worse than the combined TCC+TCN loss, our embeddings are able to achieve this without being explicitly trained for this task or taking advantage of image context. This demonstrates

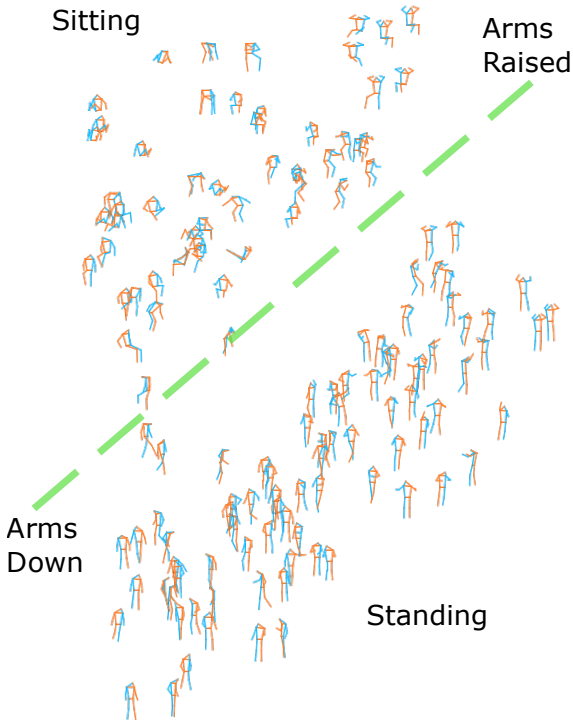


Fig. 8: Visualization of Pr-UIPE space with 2D poses in the H3.6M hold-out subset using the first two PCA dimensions. The dotted line shows the separation between sitting and standing poses.

that Pr-UIPE is applicable to aligning videos containing pose sequences.

In the last two rows of Table 6, we show the results from aligning video pairs only from the same or different views. We can see that our embedding achieves consistently high performance regardless of whether the aligned video pair is from the same or different views, which demonstrate its view-invariant property. In Fig. 7, we show visualization of synchronized action video results from different views using Pr-UIPE. More aligned videos are available at <https://drive.google.com/drive/folders/1nhPuEcX4Lhe6iK3nv84cvSCov2eJ52Xy?usp=sharing>.

5.7 Embedding Properties

5.7.1 Embedding Space Visualization

We visualize the Pr-UIPE embedding space using Principal Component Analysis (PCA). The first two principal dimensions of the 32-dimensional Pr-UIPE is shown in Fig. 8. In order to visualize unique poses, we randomly subsample the H3.6M hold-out set and select 3D poses at least 0.1 NP-MPJPE apart. Fig. 8 demon-

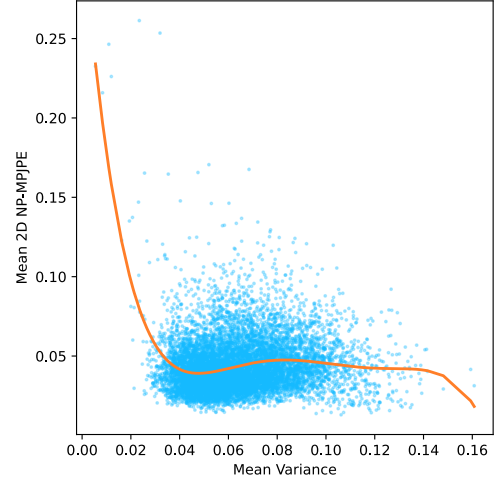


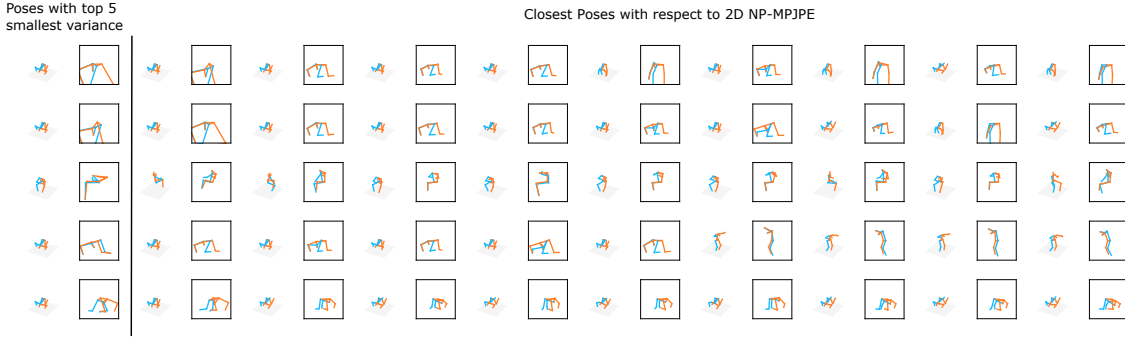
Fig. 9: Relationship between embedding variance and 2D NP-MPJPE to top-10 nearest 2D pose neighbors from the H3.6M hold-out subset. The orange curve represents the best fitting 5th degree polynomial.

strates that 2D poses from matching 3D poses are close together, while non-matching poses are further apart. Standing and sitting poses appear to be well separated from the two principle dimensions. Additionally, there are leaning poses between sitting and standing. Poses near the top-right corner of the figure have arms raised, and there is generally a gradual transition to the bottom-right corner of the figure, where arms are lowered. These results show that from 2D joint keypoints only, we are able to learn view-invariant properties with compact embeddings.

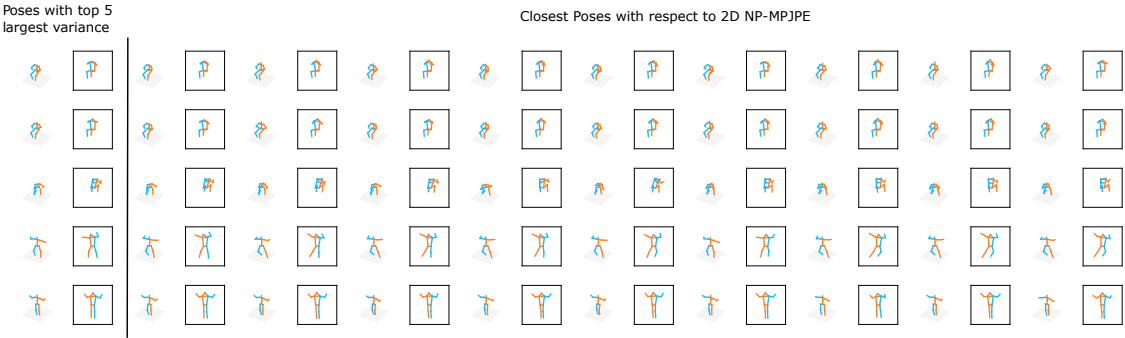
5.7.2 Effect of Variance

We study the learned embedding variance of Pr-UIPE as compared with input ambiguity. A 2D pose is ambiguous if there are similar 2D poses that can be projected from very different poses in 3D. To measure this, we compute the average 2D NP-MPJPE between a 2D pose and its top-10 nearest neighbors in terms of 2D NP-MPJPE. To ensure the 3D poses are different, we sample 10000 poses from H3.6M hold-out set with a minimum gap of 0.1 3D NP-MPJPE. If a 2D pose has small 2D NP-MPJPE to its closest neighbors, it means there are many similar 2D poses corresponding to different 3D poses. Since this 2D pose can be projected from different 3D poses, the 2D pose is ambiguous.

We sort 2D poses by their Pr-UIPE average variance across all dimensions. Fig. 10b shows that the 2D poses with the largest variances are ambiguous as they have similar 2D poses projected from different 3D poses. In contrast, we see that the closest 2D poses corresponding



(a) Poses with top-5 smallest variance and their nearest neighbors in terms of 2D NP-MPJPE.



(b) Poses with top-5 largest variance and their nearest neighbors in terms of 2D NP-MPJPE.

Fig. 10: Top retrievals by 2D NP-MPJPE from H3.6M hold-out subset for queries with top-5 largest and smallest variances. For each pose pair, the 3D pose is on the left and 2D poses are shown on the right in the boxes.

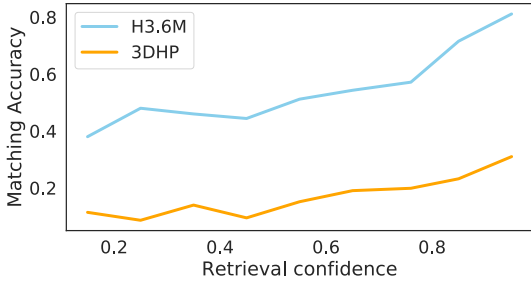


Fig. 11: Relationship between retrieval confidence and accuracy using Pr-VIPE (with camera augmentation) on H3.6M and 3DHP.

to the smallest variance poses in Fig. 10a are clearly different. Fig. 9 further shows that as the average variance increases, the 2D NP-MPJPE between similar poses generally decreases, which means that 2D poses with larger variances are more ambiguous.

5.7.3 Retrieval Confidence

We study the retrieval confidence values relative to retrieval accuracy. To do so, we randomly sample 100 queries along with their top-5 retrievals (using Pr-VIPE retrieval confidence) from each query-index camera pair. This procedure forms 6000 query-retrieval sample pairs for H3.6M (4 views, 12 camera pairs) and 55000 for 3DHP (11 views, 110 camera pairs). We bin each sample by their retrieval confidences and compute average retrieval accuracy in each bin. Fig. 11 shows the matching accuracy for each confidence bin. We can see that the accuracy positively correlates with the confidence values, which suggest our retrieval confidence is a valid indicator to model performance.

5.8 Ablation Study

5.8.1 Embedding Dimensions

Fig. 12 demonstrates the effect of embedding dimensions on retrieval accuracy on H3.6M and 3DHP. The lifting model lifts 13 2D keypoints to 3D, and therefore has a constant output dimension of 39. We see that Pr-

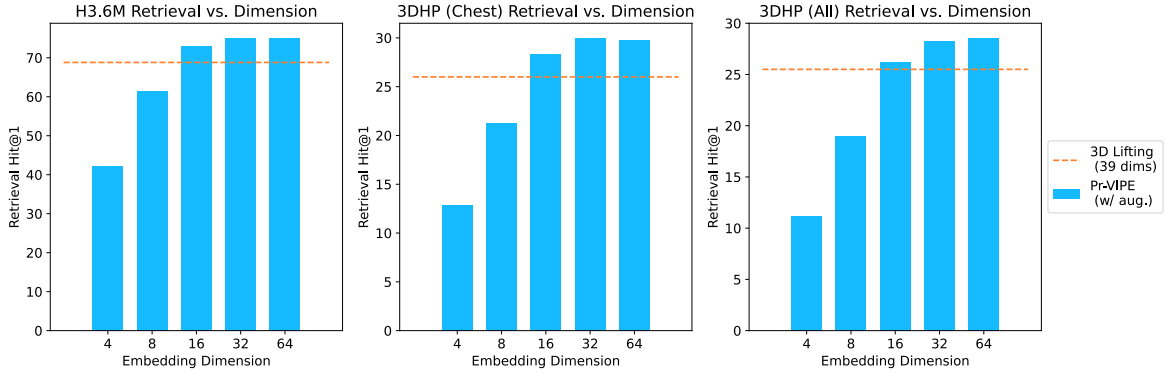


Fig. 12: Comparison of retrieval Hit@1 with different embedding dimensions on H3.6M and 3DHP. The 3D lifting baseline predicts 39 dimensions.

Table 7: Comparison of cross-view pose retrieval results Hit@1 (%) using 3D lifting and Pr-UIPE with detected and groundtruth (GT) 2D keypoints on H3.6M and 3DHP.

Model	Input Type	H3.6M	3DHP (chest)	3DHP (all)
3D lifting	Detected	68.8	26.0	25.5
	GT	90.6	52.9	51.0
Pr-UIPE	Detected	77.9	28.5	22.7
	GT	97.6	67.8	45.0

UIPE (with camera augmentation) is able to achieve a higher accuracy than lifting at 16 dimensions on all datasets. There is a further increase in accuracy as embedding dimensions increase until 32 dimensions. For all our other experiments, we use dimension 32.

5.8.2 What if 2D keypoint detectors were perfect?

We repeat our pose retrieval experiments using groundtruth 2D keypoints to simulate a perfect 2D keypoint detector on H3.6M and 3DHP. All experiments use the 4 views from H3.6M for training following the evaluation procedure in Section 5.3. Table 7 shows the results for the baseline lifting model and Pr-UIPE. These results follow the same trend as using detected keypoints inputs in Table 1. Comparing the results of detected and groundtruth keypoints, the large improvement in performance using groundtruth keypoints suggests that a considerable fraction of error in our model is due to imperfect 2D keypoint detections.

5.8.3 Effect of Number of Samples K and Margin Parameter β

Table 8 shows the effect of the number of samples K and the margin parameter β (actual triplet margin $\alpha =$

Table 8: Comparison of cross-view pose retrieval results Hit@ k (%) using Pr-UIPE (with camera augmentation) with different number of samples K and margin parameter β on H3.6M.

Hyperparameter	Value	$k = 1$	$k = 5$	$k = 10$	$k = 20$
K	10	74.8	91.5	95.1	97.3
	20	75.1	91.6	95.0	97.3
	30	74.9	91.4	95.0	97.2
	1.25	74.4	91.5	95.0	97.3
β	1.5	74.6	91.4	95.0	97.2
	2	75.1	91.6	95.0	97.3
	3	75.2	91.4	95.0	97.2

$\log \beta$) on Pr-UIPE. The number of samples control how many points we sample from the embedding distribution to compute matching probability and β controls the ratio of matching probability between matching and non-matching pairs.

By varying β , our model performance varies slightly. Table 8 shows that $\beta = 2$ and $\beta = 3$ has similar performance. The main effect of β is on retrieval confidence by controlling the scaling between matching and non-matching pairs. For larger β , non-matching pairs are scaled to a smaller matching probability.

In terms of the number of samples, Pr-UIPE performance with 10 samples is competitive with baselines, but the performance is slightly better with 20 samples. Increasing the number of samples further has similar performance. For our experiments, we use 20 samples and $\beta = 2$.

5.8.4 Effect of Camera Augmentation Parameters

We explore the effect of random rotation ranges for camera augmentation on pose retrieval in Table 9. With the same procedure as Section 5.3, all models are trained on the 4 chest-level cameras in H3.6M, and the models

Table 9: Comparison of cross-view pose retrieval results Hit@1 using Pr-UIPE with different rotation ranges for camera augmentation on H3.6M and 3DHP. The azimuth range is always $\pm 180^\circ$ and the angle ranges in the table are for elevation and roll. The row “w/o aug.” corresponds to Pr-UIPE without camera augmentation.

Hyperparameter	Range	H3.6M	3DHP (chest)	3DHP (all)
Elevation/Roll	w/o aug.	77.9	28.5	22.7
	$\pm 15^\circ$	75.7	30.5	27.2
	$\pm 30^\circ$	75.1	30.0	28.3
	$\pm 45^\circ$	74.6	29.2	28.6

Table 10: Comparison of cross-view retrieval results Hit@1 using Pr-UIPE (with camera augmentation) with different NP-MPJPE threshold κ for training and evaluation on H3.6M.

Training κ	Evaluation κ			
	0.05	0.10	0.15	0.20
0.05	45.2	75.2	90.6	96.2
0.10	44.3	75.1	90.8	96.3
0.15	41.8	73.8	90.4	96.4
0.20	39.1	72.3	90.2	96.3

with camera augmentation additionally use projected 2D keypoints from randomly rotated 3D poses. For random rotation, we always use azimuth range of $\pm 180^\circ$, and we evaluate a range of angle limits for elevation and roll.

The model without camera augmentation does the best on the H3.6M, which has the same 4 camera views as training. With increase in rotation angles during camera augmentation, the performance on chest-level cameras drop while performance on new camera views generally increases. The results demonstrate that mixing detected and projected keypoints reduces model overfitting on training camera views. Camera augmentation enables our model to generalize much better to new views.

5.8.5 Effect of NP-MPJPE threshold κ

We train and evaluate different NP-MPJPE thresholds κ in Table 10. κ determines the NP-MPJPE threshold for a matching pose pair, and Fig. 3 provides a visualization of different NP-MPJPE values.

Table 10 demonstrates that when we train with a tight threshold, e.g., $\kappa = 0.05$, we do comparatively well at looser thresholds. In contrast, when we train with a loose threshold, e.g., $\kappa = 0.20$, we do not do as well given a tighter accuracy threshold at evaluation time. This is because when we push non-matching poses using the triplet ratio loss, $\kappa = 0.20$ only pushes

Table 11: Comparison of cross-view pose retrieval results Hit@ k (%) on H3.6M targeted occlusion test sets using different training independent keypoint dropout probability q .

Evaluation type	q (%)	$k = 1$	$k = 5$	$k = 10$	$k = 20$
No occlusion	5	74.6	91.2	94.7	97.0
	10	74.1	91.1	94.7	97.1
	20	74.2	91.1	94.8	97.1
	30	73.1	90.6	94.4	96.8
	40	72.6	90.4	94.2	96.7
Targeted occlusion	5	64.2	86.5	91.7	95.2
	10	67.6	88.5	93.1	96.0
	20	68.7	88.9	93.3	96.1
	30	68.8	89.0	93.4	96.3
	40	68.7	88.9	93.3	96.2

poses that are more than 0.20 NP-MPJPE apart, and does not explicitly push poses less than the NP-MPJPE threshold. The closest retrieved pose will then be within 0.20 NP-MPJPE but it is not guaranteed to be within any threshold < 0.20 NP-MPJPE. However, when we use $\kappa = 0.05$ for training, poses that are more than 0.05 NP-MPJPE are pushed apart, which also satisfies $\kappa = 0.20$ threshold.

For all our other experiments, we use $\kappa = 0.1$. For future applications with other matching definitions, the Pr-UIPE framework is flexible and can be trained with different κ or other similarity measures to satisfy different accuracy requirements.

5.8.6 Independent Keypoint Dropout Probability

We vary the dropout probability when training Pr-UIPE (with camera augmentation) and evaluate its effect on H3.6M retrieval with fully and partially visible poses. In Table 11, we see that as training dropout probability increases, model performance generally improves on occluded poses but degrades on fully visible poses. For our main experiments, we choose to use $q = 20\%$ to tradeoff between performance on fully and partially visible poses.

6 Conclusion

We present a novel approach to learning a view-invariant, occlusion-robust probabilistic embedding for recognizing 3D human pose similarity from monocular 2D pose keypoints. We demonstrate that our embedding model, trained to recognize 3D similarity, achieves highly competitive performance on cross-view retrieval, action recognition, and video alignment against baseline models trained for each task. We also study properties of the learned embedding variance and their correlation with input ambiguity.

We further explore a synthetic occlusion augmentation strategy for model training to improve model robustness to partially visible input, without requiring diverse realistic occlusions in the training data. We show that our keypoint occlusion augmentation strategy results in a significant increase in retrieval accuracy for partially visible poses. This capability of handling incomplete input enables the use of our model for realistic photos, where body occlusion is common. It also makes it possible to devise systems for targeted partial pose search.

Pr-UIPE has a simple architecture and can be potentially applied to other domains, such as hand pose or other generic object pose recognition problems. With this work, we encourage further explorations into approaching pose related problems from an embedding learning perspective, especially where recognizing 3D similarity is central to the problem.

7 Acknowledgements

We thank Debidatta Dwibedi from Google Research, Xiao Zhang from University of Chicago, and Yisong Yue from Caltech for helpful discussions. We appreciate the support of Pietro Perona and the Computational Vision Lab at Caltech for making this collaboration possible. The author Jennifer J. Sun is supported by NSERC (funding number PGSD3-532647-2019) and Caltech.

References

1. Akhter, I., Black, M.J.: Pose-conditioned joint angle limits for 3D human pose reconstruction. In: CVPR (2015)
2. Andriluka, M., Pishchulin, L., Gehler, P., Schiele, B.: 2D human pose estimation: New benchmark and state of the art analysis. In: CVPR (2014)
3. Bojchevski, A., Günnemann, S.: Deep gaussian embedding of graphs: Unsupervised inductive learning via ranking. ICLR (2018)
4. Bromley, J., Guyon, I., LeCun, Y., Säckinger, E., Shah, R.: Signature verification using a “siamese” time delay neural network. In: NeurIPS (1994)
5. Cao, C., Zhang, Y., Zhang, C., Lu, H.: Body joint guided 3-D deep convolutional descriptors for action recognition. IEEE Transactions on Cybernetics **48**(3), 1095–1108 (2017)
6. Chen, C.H., Ramanan, D.: 3D human pose estimation = 2D pose estimation + matching. In: CVPR (2017)
7. Chen, C.H., Tyagi, A., Agrawal, A., Drover, D., Stojanov, S., Rehg, J.M.: Unsupervised 3D pose estimation with geometric self-supervision. In: CVPR (2019)
8. Chen, T., Kornblith, S., Norouzi, M., Hinton, G.: A simple framework for contrastive learning of visual representations. In: ICML (2020)
9. Chen, Y., Wang, Z., Peng, Y., Zhang, Z., Yu, G., Sun, J.: Cascaded pyramid network for multi-person pose estimation. In: CVPR (2018)
10. Chu, R., Sun, Y., Li, Y., Liu, Z., Zhang, C., Wei, Y.: Vehicle re-identification with viewpoint-aware metric learning. In: ICCV (2019)
11. Deng, J., Dong, W., Socher, R., Li, L.J., Li, K., Fei-Fei, L.: ImageNet: A large-scale hierarchical image database. In: CVPR (2009)
12. Du, W., Wang, Y., Qiao, Y.: RPAN: An end-to-end recurrent pose-attention network for action recognition in videos. In: ICCV (2017)
13. Duchi, J., Hazan, E., Singer, Y.: Adaptive subgradient methods for online learning and stochastic optimization. Journal of Machine Learning Research **12**(Jul), 2121–2159 (2011)
14. Dwibedi, D., Aytar, Y., Tompson, J., Sermanet, P., Zisserman, A.: Temporal cycle-consistency learning. In: CVPR (2019)
15. Eichner, M., Marin-Jimenez, M., Zisserman, A., Ferrari, V.: 2D articulated human pose estimation and retrieval in (almost) unconstrained still images. International Journal of Computer Vision **99**(2), 190–214 (2012)
16. Garcia-Salguero, M., Gonzalez-Jimenez, J., Moreno, F.A.: Human 3D pose estimation with a tilting camera for social mobile robot interaction. Sensors **19**(22), 4943 (2019)
17. Gu, R., Wang, G., Hwang, J.N.: Efficient multi-person hierarchical 3D pose estimation for autonomous driving. In: MIPR (2019)
18. Hadsell, R., Chopra, S., LeCun, Y.: Dimensionality reduction by learning an invariant mapping. In: CVPR (2006)
19. He, K., Gkioxari, G., Dollár, P., Girshick, R.: Mask R-CNN. In: CVPR (2017)
20. He, X., Zhou, Y., Zhou, Z., Bai, S., Bai, X.: Triplet-center loss for multi-view 3D object retrieval. In: CVPR (2018)
21. Hermans, A., Beyer, L., Leibe, B.: In defense of the triplet loss for person re-identification. arXiv preprint arXiv:1703.07737 (2017)
22. Ho, C.H., Morgado, P., Persekian, A., Vasconcelos, N.: PIEs: Pose Invariant Embeddings. In: CVPR (2019)
23. Hu, W., Zhu, S.C.: Learning a probabilistic model mixing 3D and 2D primitives for view invariant object recognition. In: CVPR (2010)
24. Huang, C., Loy, C.C., Tang, X.: Local similarity-aware deep feature embedding. In: NeurIPS (2016)
25. Ionescu, C., Papava, D., Olaru, V., Sminchisescu, C.: Human3.6M: Large scale datasets and predictive methods for 3D human sensing in natural environments. IEEE Transactions on Pattern Analysis and Machine Intelligence **36**(7), 1325–1339 (2013)
26. Iqbal, U., Garbade, M., Gall, J.: Pose for action - Action for pose. In: FG (2017)
27. Iscen, A., Tolias, G., Avrithis, Y., Chum, O.: Mining on manifolds: Metric learning without labels. In: CVPR (2018)
28. Isakov, K., Burkov, E., Lempitsky, V., Malkov, Y.: Learnable triangulation of human pose. In: ICCV (2019)
29. Jammalamadaka, N., Zisserman, A., Eichner, M., Ferrari, V., Jawahar, C.: Video retrieval by mimicking poses. In: ACM MM (2012)
30. Ji, X., Liu, H.: Advances in view-invariant human motion analysis: A review. IEEE Transactions on Systems, Man, and Cybernetics, Part C (Applications and Reviews) **40**(1), 13–24 (2009)
31. Ji, X., Liu, H., Li, Y., Brown, D.: Visual-based view-invariant human motion analysis: A review. In: KES (2008)

32. Kendall, A., Gal, Y.: What uncertainties do we need in Bayesian deep learning for computer vision? In: NeurIPS (2017)
33. Kingma, D.P., Welling, M.: Auto-encoding variational Bayes. In: ICLR (2014)
34. Kipf, T.N., Welling, M.: Semi-supervised classification with graph convolutional networks. In: ICLR (2017)
35. Kocabas, M., Karagoz, S., Akbas, E.: Self-supervised learning of 3D human pose using multi-view geometry. In: CVPR (2019)
36. LeCun, Y., Huang, F.J., Bottou, L., et al.: Learning methods for generic object recognition with invariance to pose and lighting. In: CVPR (2004)
37. Li, J., Wong, Y., Zhao, Q., Kankanhalli, M.: Unsupervised learning of view-invariant action representations. In: NeurIPS (2018)
38. Li, S., Ke, L., Pratama, K., Tai, Y.W., Tang, C.K., Cheng, K.T.: Cascaded deep monocular 3D human pose estimation with evolutionary training data. In: CVPR (2020)
39. Lin, T.Y., Maire, M., Belongie, S., Hays, J., Perona, P., Ramanan, D., Dollár, P., Zitnick, C.L.: Microsoft COCO: Common objects in context. In: ECCV (2014)
40. Liu, J., Akhtar, N., Ajmal, M.: Viewpoint invariant action recognition using RGB-D videos. *IEEE Access* **6**, 70061–70071 (2018)
41. Liu, M., Yuan, J.: Recognizing human actions as the evolution of pose estimation maps. In: CVPR (2018)
42. Luvizon, D.C., Tabia, H., Picard, D.: Multi-task deep learning for real-time 3D human pose estimation and action recognition. *IEEE Transactions on Pattern Analysis and Machine Intelligence* (2020)
43. von Marcard, T., Henschel, R., Black, M., Rosenhahn, B., Pons-Moll, G.: Recovering accurate 3D human pose in the wild using IMUs and a moving camera. In: ECCV (2018)
44. Martinez, J., Hossain, R., Romero, J., Little, J.J.: A simple yet effective baseline for 3D human pose estimation. In: ICCV (2017)
45. Mehta, D., Rhodin, H., Casas, D., Fua, P., Sotnychenko, O., Xu, W., Theobalt, C.: Monocular 3D human pose estimation in the wild using improved CNN supervision. In: 3DV (2017)
46. Misra, I., Zitnick, C.L., Hebert, M.: Shuffle and learn: Unsupervised learning using temporal order verification. In: ECCV (2016)
47. Mori, G., Pantofaru, C., Kothari, N., Leung, T., Toderici, G., Toshev, A., Yang, W.: Pose embeddings: A deep architecture for learning to match human poses. *arXiv preprint arXiv:1507.00302* (2015)
48. Nie, B.X., Xiong, C., Zhu, S.C.: Joint action recognition and pose estimation from video. In: CVPR (2015)
49. Oh, S.J., Murphy, K., Pan, J., Roth, J., Schroff, F., Gallagher, A.: Modeling uncertainty with hedged instance embedding. In: ICLR (2019)
50. Oh Song, H., Xiang, Y., Jegelka, S., Savarese, S.: Deep metric learning via lifted structured feature embedding. In: CVPR (2016)
51. Ong, E.J., Micilotta, A.S., Bowden, R., Hilton, A.: Viewpoint invariant exemplar-based 3D human tracking. *Computer Vision and Image Understanding* **104**(2-3), 178–189 (2006)
52. Oord, A.v.d., Li, Y., Vinyals, O.: Representation learning with contrastive predictive coding. In: NeurIPS (2018)
53. Papandreou, G., Zhu, T., Chen, L.C., Gidaris, S., Tompson, J., Murphy, K.: PersonLab: Person pose estimation and instance segmentation with a bottom-up, part-based, geometric embedding model. In: ECCV (2018)
54. Papandreou, G., Zhu, T., Kanazawa, N., Toshev, A., Tompson, J., Bregler, C., Murphy, K.: Towards accurate multi-person pose estimation in the wild. In: CVPR (2017)
55. Parkhi, O.M., Vedaldi, A., Zisserman, A.: Deep face recognition. In: BMVC (2015)
56. Pavlo, D., Feichtenhofer, C., Grangier, D., Auli, M.: 3D human pose estimation in video with temporal convolutions and semi-supervised training. In: CVPR (2019)
57. Qiu, H., Wang, C., Wang, J., Wang, N., Zeng, W.: Cross view fusion for 3D human pose estimation. In: ICCV (2019)
58. Rao, C., Shah, M.: View-invariance in action recognition. In: CVPR (2001)
59. Rayat Imtiaz Hossain, M., Little, J.J.: Exploiting temporal information for 3d human pose estimation. In: ECCV (2018)
60. Rhodin, H., Salzmann, M., Fua, P.: Unsupervised geometry-aware representation for 3D human pose estimation. In: ECCV (2018)
61. Rhodin, H., Spörri, J., Katircioglu, I., Constantin, V., Meyer, F., Müller, E., Salzmann, M., Fua, P.: Learning monocular 3D human pose estimation from multi-view images. In: CVPR (2018)
62. Ronchi, M.R., Kim, J.S., Yue, Y.: A rotation invariant latent factor model for moveme discovery from static poses. In: ICDM (2016)
63. Schroff, F., Kalenichenko, D., Philbin, J.: FaceNet: A unified embedding for face recognition and clustering. In: CVPR (2015)
64. Sermanet, P., Lynch, C., Chebotar, Y., Hsu, J., Jang, E., Schaal, S., Levine, S., Brain, G.: Time-contrastive networks: Self-supervised learning from video. In: ICRA (2018)
65. Sun, J.J., Zhao, J., Chen, L.C., Schroff, F., Adam, H., Liu, T.: View-invariant probabilistic embedding for human pose. *ECCV* (2020)
66. Sun, X., Xiao, B., Wei, F., Liang, S., Wei, Y.: Integral human pose regression. In: ECCV (2018)
67. Tekin, B., Márquez-Neila, P., Salzmann, M., Fua, P.: Learning to fuse 2D and 3D image cues for monocular body pose estimation. In: ICCV (2017)
68. Tome, D., Toso, M., Agapito, L., Russell, C.: Rethinking pose in 3D: Multi-stage refinement and recovery for markerless motion capture. In: 3DV (2018)
69. Vilnis, L., McCallum, A.: Word representations via gaussian embedding. In: ICLR (2015)
70. Wang, J., Song, Y., Leung, T., Rosenberg, C., Wang, J., Philbin, J., Chen, B., Wu, Y.: Learning fine-grained image similarity with deep ranking. In: CVPR (2014)
71. Wohlhart, P., Lepetit, V.: Learning descriptors for object recognition and 3D pose estimation. In: CVPR (2015)
72. Wu, C.Y., Manmatha, R., Smola, A.J., Krahenbuhl, P.: Sampling matters in deep embedding learning. In: ICCV (2017)
73. Xia, L., Chen, C.C., Aggarwal, J.K.: View invariant human action recognition using histograms of 3D joints. In: CVPRW (2012)
74. Zeng, A., Sun, X., Huang, F., Liu, M., Xu, Q., Lin, S.: SRNet: Improving generalization in 3D human pose estimation with a split-and-recombine approach. In: ECCV (2020)
75. Zhang, W., Zhu, M., Derpanis, K.G.: From actemes to action: A strongly-supervised representation for detailed action understanding. In: ICCV (2013)
76. Zhao, L., Peng, X., Tian, Y., Kapadia, M., Metaxas, D.N.: Semantic graph convolutional networks for 3D human pose regression. In: CVPR (2019)

-
77. Zheng, L., Huang, Y., Lu, H., Yang, Y.: Pose invariant embedding for deep person re-identification. *IEEE Transactions on Image Processing* **28**, 4500–4509 (2019)
 78. Zhou, X., Huang, Q., Sun, X., Xue, X., Wei, Y.: Towards 3D human pose estimation in the wild: A weakly-supervised approach. In: *ICCV* (2017)

A Keypoint Definition

Fig. 13 illustrates the keypoints that we use in our experiments. The 16 keypoints we use to define a 3D pose are shown in Fig. 13a. We map 3D keypoints from different datasets to these 16 keypoints for training and evaluation in this paper. Besides most unambiguous mappings, several special mappings that we would like to note here are:

- For the Human3.6M dataset [25], we discard the "Neck-/Nose" keypoint and map the "Thorax" keypoint to "Neck".
- For the MPII-3DHP dataset [45], we discard the "Head top" keypoint.
- For the 3DPW dataset [43], we add "Pelvis" keypoint as the center of "Left hip" and "Right hip", and add "Spine" as the center of "Pelvis" and "Neck".

The 13 2D keypoints we use to define a 2D pose are shown in Fig. 13b. We follow the COCO [39] keypoint definition, keeping all the 12 body keypoints and the "Nose" keypoint on the head.

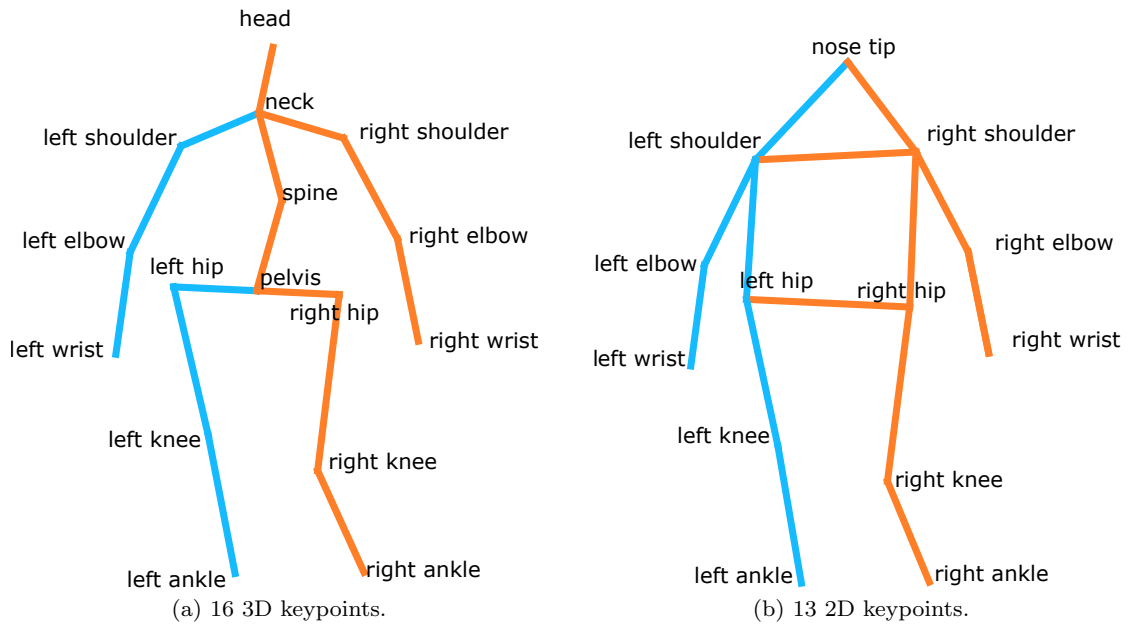


Fig. 13: Definitions of pose keypoints.